**Proceedings of the 18th International Symposium on the
Packaging and Transportation of Radioactive Materials
PATRAM 2016
September 18-23, 2016, Kobe, Japan**

Paper No. 5001   Spent Nuclear Fuel Transport Reliability Study[*]

Jy-An John Wang, Hong Wang, Hao Jiang
Oak Ridge National Laboratory
Oak Ridge, Tennessee, 37830, USA

Abstract

SNF rods lie horizontally and are supported by the assembly guide tubes and spacer grids inside specially designed transportation casks. During normal conditions of transport (NCT), these fuel rods are subjected to oscillatory bending due to inertial effects. This oscillatory bending is the major vibrational load of SNF rods as discussed in 10 CFR §71.71. Besides the change in composite structure of fuel pellets and cladding that occurs during irradiation, the SNF rods typically have burnup induced damage (pores and micro cracks), oxide and hydride layers, residual stresses, altered interfaces, and trapped fission products. Understanding the impact these changes may have on the strength of the SNF fuel/cladding system is required to accurately simulate the performance of SNF rods during transport.

The objective of this research is to collect dynamic experimental data on spent nuclear fuel (SNF) under simulated transportation environments using the Cyclic Integrated Reversible-Bending Fatigue Tester (CIRFT), the hot-cell testing technology developed at Oak Ridge National Laboratory (ORNL). The collected CIRFT data will be utilized to support ongoing spent fuel modeling activities, and support SNF transportation related licensing issues. Recent testing to understand the effects of hydride reorientation on SNF vibration integrity is also being evaluated.

CIRFT results have provided insight into the fuel/clad system response to transportation related loads. The major findings of CIRFT on the high-burnup (HBU) SNF are as follows:

- SNF system interface bonding plays an important role in SNF vibration performance,
- Fuel structure contributes to the SNF system stiffness,
- There are significant variations in stress and curvature of SNF systems during vibration cycles resulting from segment pellets and clad interaction, and
- SNF failure initiates at the pellet-pellet interface region and appears to be spontaneous.

Because of the non-homogeneous composite structure of the SNF system, finite element analyses (FEA) are needed to translate the global moment-curvature measurement into local stress-strain profiles. The detailed mechanisms of the pellet-pellet and pellet-clad interactions and the stress concentration effects at the pellet-pellet interface cannot be readily obtained directly from a CIRFT system measurement. Therefore, detailed FEA is used to understand the global test response, and that data will also be presented.

## I. INTRODUCTION

Transportation packages for spent nuclear fuel (SNF) must meet safety requirements specified by federal regulations. For normal conditions of transport, vibration loads incident to transport must be considered. This is particularly relevant for high-burnup fuel (>45 GWd/MTU). As the burnup of the fuel increases, a number of changes occur that may affect the performance of the fuel and cladding in storage and during transportation. Spent fuel cladding has traditionally provided defense-in-depth as the primary fission product barrier in the nuclear fuel cycle, and has been relied upon to provide geometry control for criticality safety during transportation. The mechanical properties of high-burnup de-fueled cladding have been previously studied by subjecting defueled cladding tubes to longitudinal (axial) tensile tests, ring-stretch tests, ring-compression tests, and biaxial tube burst tests. The objective of this study is to investigate the mechanical properties and behavior of both the cladding and the fuel in the cladding (including inertia induced fuel pellet and clad interaction) under vibration/cyclic loads similar to the sustained vibration loads experienced during normal transport. [1]

The PWR fuel assembly skeleton [2], as shown in Fig. 1, is formed by guide tubes and spacer grids designed to constrain fuel rods during a reactor operation. In a vertical service setup, the skeleton is subjected to vibration loads induced by fluid dynamics, and the rods' dead weight is transmitted through the spacer grids to the guide tubes during reactor operation. When the SNF assembly is in a horizontal orientation for NCT, the skeleton formed by the guide tubes and spacer grids becomes the primary load-bearing system that carries and transfers the vibration loads within an SNF assembly. This includes interaction of forces between the SNF assembly and the canister basket walls.

In an EPRI Synthesis Report-1015048 [3], the plastic collapse of the spacer grids and the breakage of the guide tubes were considered as the two modes for evaluating fuel assembly damage. Therefore, the integrity of guide tubes and spacer grids during transport requires full attention since it will affect the dynamic load transmitting mechanism within the fuel assembly and will consequently dictate the multipurpose purpose canister (MPC) design concept to ensure safe SNF transport.

| Fuel assembly | Guide tubes and spacer grids [2] |
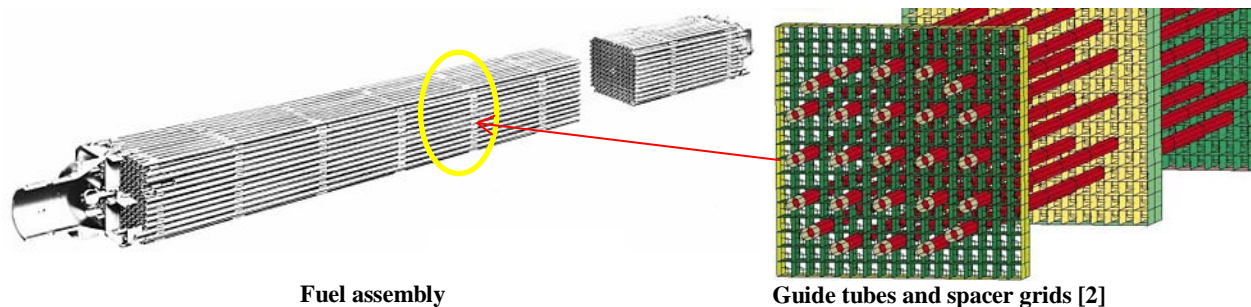
Fig. 1. Schematic of 17 × 17 PWR fuel assembly.

Random vibration registered at the SNF transport cask, which is excited from the railcar bed, provides the external loading driver to vibrate the SNF assembly. In addition to this external vibration driver, the fuel assembly also registers internal transient shocks resulting from the dynamic interactions among the fuel assembly components inside the cask. These components include the skeleton, fuel rods, and canister basket walls. Their dynamic interactions can significantly increase the high-rate impact loading frequency within fuel assembly components during NCT. Sandia National Laboratories (SNL) registered maximum 22 g peak vertical vibration acceleration at mid span of the surrogate rod adjacent to the spacer grid from the accelerometer reading during the truck transportation test [4]. In contrast, the maximum vertical acceleration of 5.6 g was registered on the top of transport basket at mid-span.

Furthermore, the aged or fatigued skeleton has the potential to increase the gap population and intensity within the fuel assembly system. The consequence of increased gap potential is the increase in contact

impact loading intensity between the fuel rods, the skeleton, and the basket wall. The contact interactions between fuel rods, spacer grids, and basket wall can also increase fuel rod transient shock load frequencies. Thus, external cask vibration needs to be mitigated, along with internal amplification from the fuel assembly system vibration and its contact-interaction transient shocks [5]. System damping may need to be increased to reduce vibration intensity. Such mitigations will eventually impact the design of the canister system.

The vibration loads experienced by SNF rods during transportation can be characterized by dynamic, cyclic, bending loads. The transient vibration signals in a specified transport environment can be analyzed, and frequency, amplitude and phase components of the vibration can be identified. The methodology being developed at Oak Ridge National Laboratory (ORNL) is a novel approach to support the study of the vibration integrity of actual SNF rod segments through the testing and evaluation of the fatigue performance of SNF rods at target NCT loads, including the harmonic vibration as well as contact interactions induced transient shocks. ORNL has developed a cyclic integrated reversible pure bending fatigue tester (CIRFT), shown in Fig. 2, to evaluate the response of the SNF rods under harmonic vibration loads as noted in Refs 6-11. The schematic diagram to illustrate how to use CIRFT test to assist the SNF effective lifetime evaluation under NCT is shown in Fig. 3.
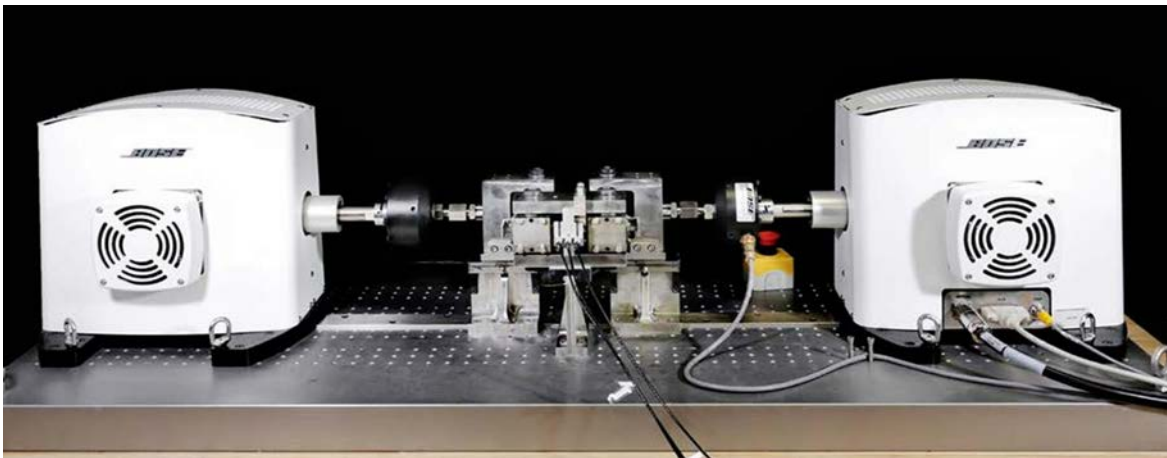

Fig. 2 Cyclic integrated reversible-bending fatigue tester; SNF is loaded in the central U-bent fixture.

A three-point deflection measurement technique using linear variable differential transformers (LVDTs) is used to characterize the rod curvature of samples under test conditions, and electromagnetic force linear motors are used as the driving system to provide the mechanical load. ORNL CIRFT system has been successfully operated in a hot cell since fall 2013, to perform SNF vibration testing on high burnup fuel to evaluate the effect of pellet-clad interaction and effects of pellet-pellet-clad interface bonding efficiency on the effective lifetime of the fuel-clad structure bending fatigue performance.
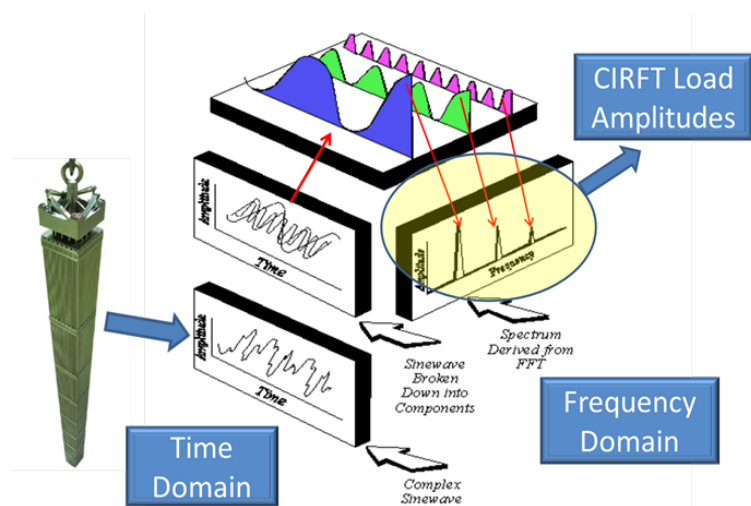

Fig. 3 CIRFT Methodology to determine SNF effective lifetime using SNF vibration time-history data.

Since the CIRFT commission in the hot-cell, we have been collected the experimental data on SNF from pressurized water reactors (PWRs), including H. B. Robinson (HBR) and North Anna (NA) Zircaloy-4 cladding and NA and Catawba M5 cladding, and the Limerick Generating Station boiling water reactor (BWR) under simulated transportation environments using the CIRFT Tester [12-14].

Testing on SNF rods from PWRs—HBR and NA Zircaloy-4 cladding and Catawba M5 cladding [6-8]—demonstrated that the cyclic fatigue lifetime of SNF rods generally depends on the amplitude of applied moment when a 5 Hz waveform is used. It was also demonstrated that the lifetime of SNF is related to the degree of damage to cladding and fuel pellets resulting from irradiation after a long term of service inside a reactor, as well as the loading amplitude and loading rate, due to different fatigue damage mechanisms triggered by the intensity of pellet-clad mechanical interaction. CIRFT study further extended the vibration data collected to include Zircaloy-2 data from a BWR environment in 2015. An S-N trend similar to that of the PWR data was also observed in the BWR data [15]. Furthermore, from CIRFT test data the accumulated damage from the combination of low-amplitude CIRFT cyclic bending plus transient shocks (high-amplitude bending load) indicates an accelerated aging effect compared to that of low-amplitude cyclic bend loading alone. In 2016 CIRFT test has also been extended to SNF hydride reorientation effect study. Moreover, the detailed HBU HBR CIRFT data was published in NUREG/CR-7198 [1].

II. TEST METHOD CONCEPT

The objective of this testing program is to develop testing protocols to evaluate the bending deformation responses and the associated fatigue mechanical properties for HBU fuel rods relevant to transportation conditions. Thus, the HBU fuel rods would be tested in a condition and geometry as close as possible to NCT. Currently, most of the mechanical testing devices require a specified specimen design, such as a pre-notch or reduced gage section, to prevent failure at the grip location and ensure meaningful data. For this testing program, it was recommended that the test segment not be altered by machining a gage section. Therefore, an innovative U-frame and grip design were developed. Cost considerations also had a significant influence on the development of the testing program. Hot-cell space and time are extremely limited and costly, as is testing material. For this testing program, we wanted to use a small test segment, design a compact test device, and develop a test protocol for efficient testing. Finally, the curvature response of the test segment needed to be measured with as little interpretation as possible. It was not practical to weld strain gauges onto the segments or use lasers to measure deflection on HBU material in a hot cell. Therefore, three adjacent linear variable differential transformers (LVDTs) were used to measure lateral deflections of the test specimen, see Fig. 4, so that the curvature of the specimen could be calculated without interpretation or assumptions regarding the deformation of various components of the testing system.
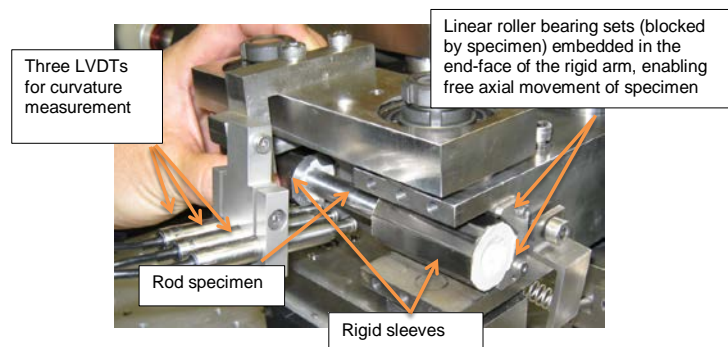

Fig. 4 Three LVDTs location at CIRFT gage section.

As regarding CIRFT specimen preparation, the mounting of rigid sleeves onto the rod is achieved using casting epoxy. The cast epoxy, therefore, serves as the compliant layer whose size depends on the dimensions of the rigid sleeve and rod. Casting of the epoxy has been proven feasible in the hot cell environment. A vise mold has been designed and built for that purpose, and the procedures to cast the epoxy and mount the rigid sleeves into the rod specimen in a hot cell have also been developed [1, 10].

4

III. TEST PROTOCOL AND EXPERIMENTAL DEMONSTRATION

3.1   Static Testing

The purpose of static testing is to generate bending strength data for SNF rods. In particular, the static tests measure the bending strength of *fueled* SNF rods so that the contribution of the fuel to the SNF rod bending strength can be evaluated. The analysis of the static test results also provides a reference yield strength to establish the dynamic testing matrix. Static testing is carried out using displacement control. It involves ramping both loading arms of the U-frame at 0.1 mm/s up to 12 mm, where 12 mm displacement is the machine stroke capacity. The following procedure is followed.

- Perform the standard static bending test beyond SNF rod yielding to failure or up to device displacement or loading capacity.
- If the machine capacity is reached before specimen failure or specimen maximum strength is reached, repeat unidirectional static testing using the same condition for a few more loading/unloading cycles, or to specimen failure, whichever comes first.
- If the SNF rod does not fail after 3–4 loading/unloading cycles, follow a dynamic or cyclic test procedure to fracture the tested specimen to support postmortem examination. Such a dynamic test is called a follow-up test.
- Collect and weigh any fuel fragments that may have dislodged during the test.

The loading processes to be used after the first loading cycle were suggested because the device might not have sufficient stroke to test these particular specimens to failure.

3.2   Dynamic Testing

Dynamic testing consists of two major activities—dynamic real-time online monitoring and periodic quasi-static deformation measurements (see Fig. 5). The procedure is as follows:

- Perform the dynamic cyclic test under constant load control using a sine wave input in reverse bending mode.
- Set the cycle frequency at 5 Hz and select the amplitudes for individual cycle tests considering the target cycles to be achieved with each test.
- Monitor the SNF fatigue evolution with defined intervals: perform static measurements of the rod deformation at the end of each target cycle with a frequency of 0.05 Hz and appropriate amplitude under displacement control.
- Stop the dynamic test when failure/clad fracture is detected or the preselected number of cycles is reached.
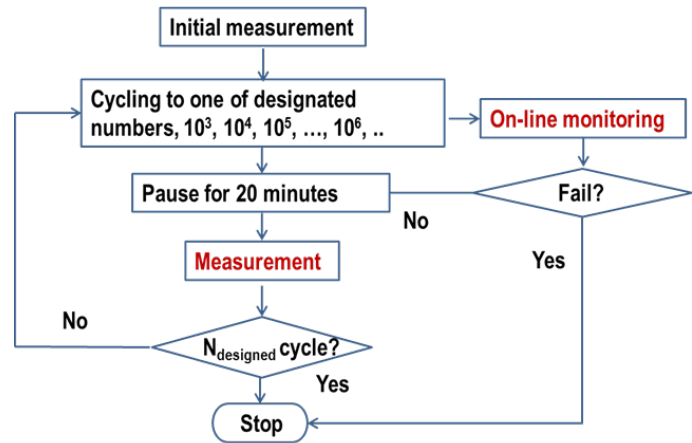- Weigh any fuel fragments that fall out of the fracture.

Fig. 5. Flowchart for cyclic testing of spent fuel rod.

3.3   Data Processing

Measurement data and online monitoring data are converted into the applied moment and curvature, based on the load channel (load1 and load2) information, the loading arm length (101.60 mm), and LVDT

data (LVDT1, 2, and 3). This information is used to generate the time series plots of moment and curvature and the moment-curvature hysteresis loops, such as those illustrated in

Fig. for D1. The uniform moment applied to the rod is derived simply from the following equation.

$$M = F \times L \tag{1}$$

where F is the averaged value of applied loads (load1 and load2) from the Bose dual motors, and L is the loading arm length, 101.60 mm. The computation of curvature k is described in Section 2.3.
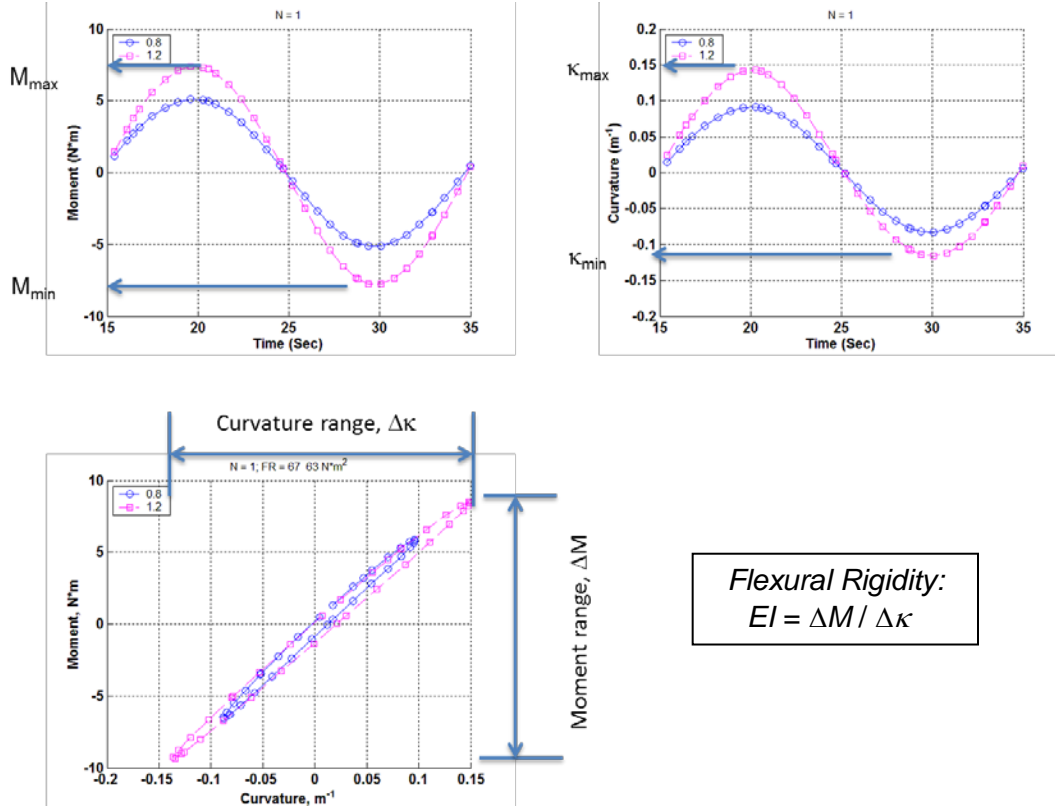

Fig.6. Moment, curvature time series, and moment-curvature hysteresis loop for rod D1. Two measurements are displayed with relative displacement 0.8 and 1.2 mm at the loading points of U-frame.

An equivalent stress-strain curve can be obtained under the assumption that the SNF rod can be idealized as a linear elastic homogeneous material without consideration of the effects induced by pellet-cladding interaction. The equivalent stress was calculated using:

$$\sigma = M \times y_{max}/I \tag{2}$$

where I is the moment of inertia, $I = I_c + I_p$, I_c and I_p are moments of inertia of cladding and pellet, respectively, and y_{max} is the maximum distance to the neutral axis of the test rod section and is set equal to the radius of the cladding. The measured ODs of rod segments are given in Table 2. The calculation of stress disregards the difference of elastic moduli between cladding and pellets.

The equivalent strain is then:

$$\varepsilon = k \times y_{man}. \tag{3}$$

6

3.3.1 HBU SNF Characteristics

The SNF system contains multiphase components such as the cladding, pellets, and oxide. Thus, an SNF rod is far from an ideal homogeneous material, especially in HBU fuel, where the irradiated cladding and pellets and the associated interfaces are modified significantly during irradiation. Assuming the HBU rod has a perfect interface bond at pellet-cladding and pellet-pellet interfaces, the associated flexural rigidity EI can be expressed as

$$EI = E_c I_c + E_p I_p \,, \tag{4}$$

where I_c and I_p are moments of inertia of the cladding and pellet, respectively, and the value of I_p is based on the reference. E_c and E_p are the Young's modulus of the cladding and pellet. The associated stress and strain evaluations of Eqs. (3) and (4) can still be used.

However, because of the imperfect interface cohesive bonding, the effective EI will be less than that of the perfect bonding property, which can be written as

$$EI = E_c I_c + E_p I_p - F(BE, \text{cladding, fuel}), \tag{5}$$

where F is the correction factor, which depends on interface bonding efficiency (BE) and the fuel pellet and cladding aging properties, as well as cyclic loading amplitudes. This hypothesis was further validated in Reference 17.

Generally, the moment range (ΔM), curvature range ($\Delta \kappa$), and flexural rigidity EI are used in characterizing the mechanical properties of the fuel rod. These are defined as:

$$\Delta M = M_{max} - M_{min}, \ \ \Delta \kappa = \kappa_{max} - \kappa_{min},$$

$$EI = \Delta M / \Delta \kappa \tag{6}$$

where the subscripts "max" and "min" represent the maximum and minimum waveforms (Fig. 6).

IV. CIRFT STATIC TESTING RESULTS

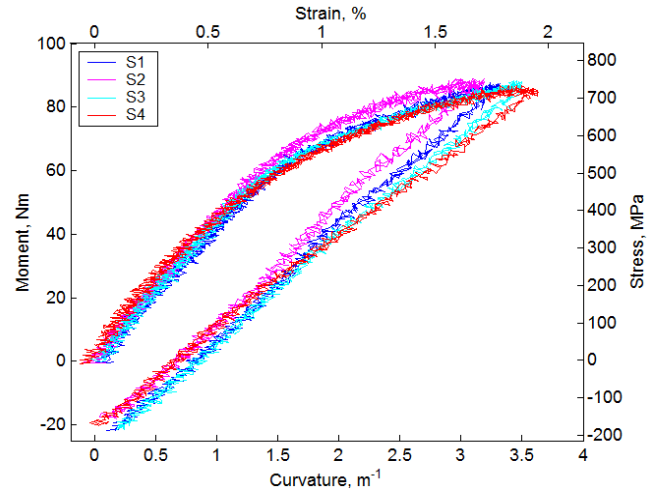### 4.1 H. B. Robinson (HBR) SNF Rod Test Results

Three specimens were tested under static loading in the hot cell for test system benchmarking. Four static tests, S1 to S4, were subsequently conducted. In the static tests reported above, loading/unloading cycles did not result in apparent or catastrophic failure of specimens because of the limited stroke of the CIRFT machine. The failure of specimens occurred in the initial loading cycle of two benchmarking tests, Scal1 and Scal2. The peak moments of the two tests were 78.2 and 80.7 N·m, respectively.

For the four static test samples, since the machine capacity was reached and no failure occurred to the specimen, a follow-up dynamic test was conducted with reversible bending under ±25.40 to 30.48 N·m at 5 Hz. The purpose of this procedure was to test the specimen to failure for further postmortem examination.

A summary of the moment-curvature curves is shown in Fig. 7. for the four static tests. The top and right axes present the scale of the converted maximum strain and stress of the bending specimen according to Eqs. (2) and (3). Several important observations can be made with respect to the responses of the test specimens during the first loading cycle.

- The static test results of the four specimens prior to the follow-up dynamic testing all show relatively similar elastic behavior.
- The initial moment-curvature response is characterized by a flexural rigidity of 52 to 63 N·m^2.

- There is a change in the flexural rigidity at the moment of 12 to 21 N·m. This change will be quantified in Section 3.2.
- After this change, the moment-curvature response is characterized by a degraded flexural rigidity of 37 to 41 N·m^2.
- Each static test segment experienced 1–2% plastic strain without failure.
- The unloading flexural rigidity is similar to the loading flexural rigidity in the second stage after the moment reaches 12 to 21 N·m.
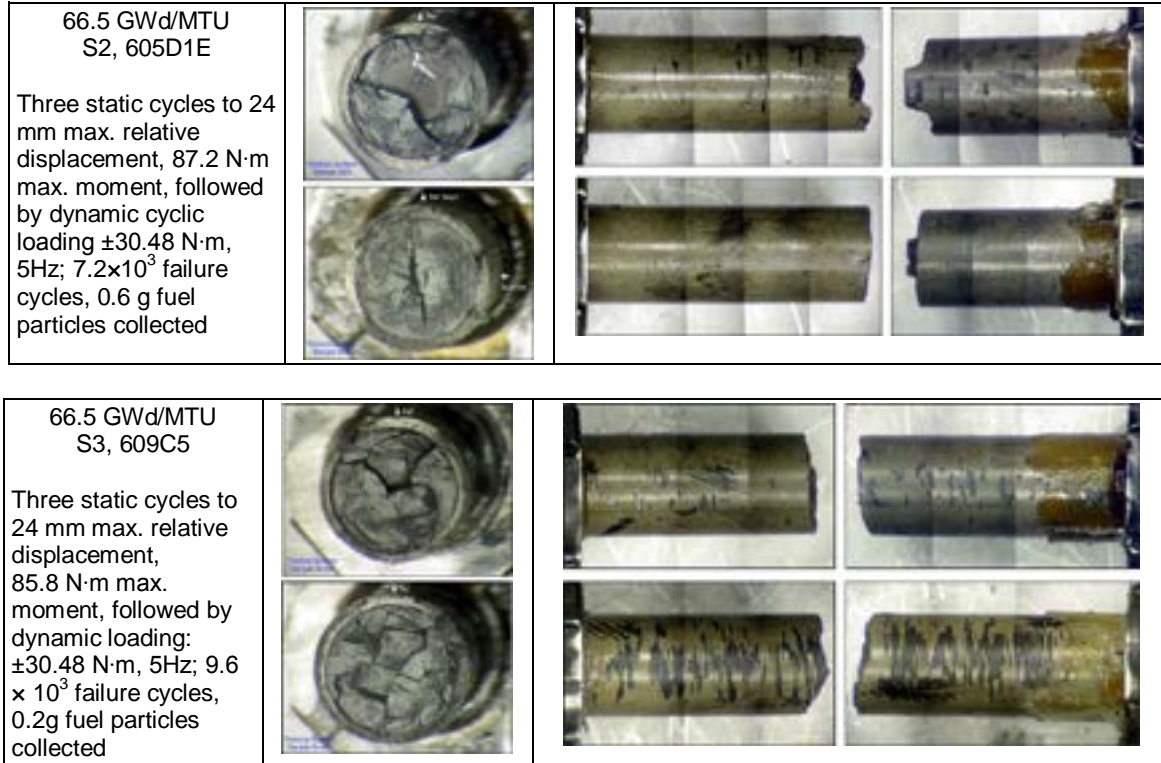
Overall, the rods failed within the gage sections in all of the tested rods. The majority of the rod fractures involved the pellet-to-pellet interfaces (PPIs). S3 was exceptional in that the failure location seemed away from pellet-pellet interface, as no end face of the pellet can be identified from the fracture surface of the fuel.

Fig. 7 Moment-curvature curves measurements in static tests (Corresponding stress and strain displayed on right and top axes, respectively).

4.1.2   *Postmortem Examination*

The postmortem results for specimens S2 and S3 are shown in Fig. 8.

| 66.5 GWd/MTU S2, 605D1E

Three static cycles to 24 mm max. relative displacement, 87.2 N·m max. moment, followed by dynamic cyclic loading ±30.48 N·m, 5Hz; 7.2×10^3 failure cycles, 0.6 g fuel particles collected | |
| 66.5 GWd/MTU S3, 609C5

Three static cycles to 24 mm max. relative displacement, 85.8 N·m max. moment, followed by dynamic loading: ±30.48 N·m, 5Hz; 9.6×10^3 failure cycles, 0.2g fuel particles collected | |

Fig. 8 Postmortem examination on static test samples, S2 and S3. [1]

8

4.1.3   Characteristics of Moment-Curvature Curve

The moment-curvature responses of all four static test specimens were similar. They are characterized by two linear constituent behavior responses, followed by a nonlinear response during the loading and a linear response upon unloading. It was observed that when reloaded, the rod followed the unloading curve linearly and proceeded with nonlinear response after passing the previously achieved maximum load. Such loading/unloading/reloading responses can be found in many mechanical systems where strain hardening prevails.

An effort was made to characterize the moment-curvature response based on the characteristic points to facilitate understanding test results. The flexural rigidities EI1, EI2, and EI3 were obtained, corresponding to the slopes of the first and second linear segments and of the unloading segment by using curve fitting with the first order polynomial (Fig. 9). The characteristic curvatures and moments at the slopes' changed points A and B were then identified. In addition, the moment at point C corresponding to a 0.37 m^{-1} irreversible curvature, or 0.2% equivalent plastic strain, was found by using a line with the same slope as that of unloading and horizontal axis intercept 0.37 m^{-1}. The quantities corresponding to points A, B, and C are designated by k_A, k_B, k_C, and M_A, M_B, and M_C.

Fig. 9. Characteristic points of moment-curvature curve.

4.1.4   Comparison of Static Results with PNNL Cladding Data

In order to investigate the contribution of fuel pellets in the fuel rod structure, analysis was performed to compare the measured static results to predicted values considering cladding alone. The cladding properties used for this analysis were obtained from a database maintained by PNNL [16]. The hypothetical "cladding only" moment-curvature response was plotted together with the moment-curvature response of the high burnup fuel rod system as shown in Fig. 10, where the SNF rod shows much higher bending moment resistance compared to that of PNNL data with cladding alone. A comparison of CIRFT testing results with cladding-only rigidity based on PNNL data is given in Table 1, with HBR's rod dimensions.
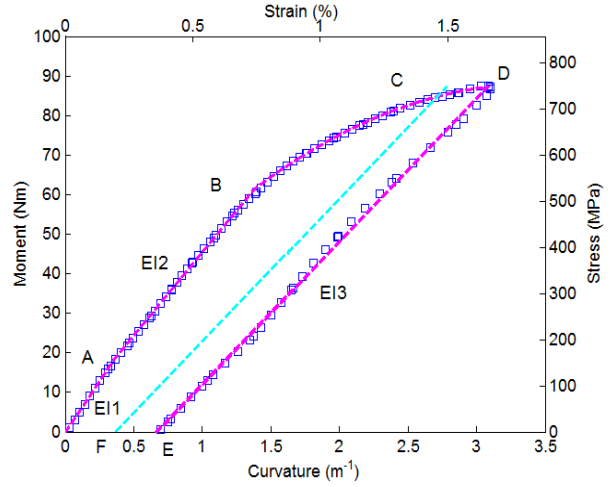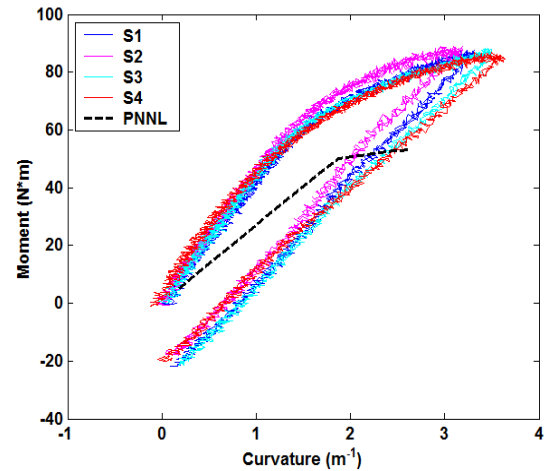

Fig. 10 Comparison of CIRFT global data with PNNL moment-curvature curve converted from PNNL data.

Table 1. Comparison of flexural rigidity results between CIRFT testing and PNNL data

	EI1 (N·M²)	EI2 (N·M²)	EI3 (N·M²)
CIRFT testing	54.751	39.944	33.090
PNNL data	26.933		

4.2 Static Testing of North Anna M5™ SNF

4.2.1 NA3/651D3

The static test was conducted on the specimen with the CIRFT label NA3 (fuel segment 651D3) under a displacement control mode using the following test procedure:

- Ramp up to 12.00 mm at 0.1 mm/s rate at each loading point or each Bose motor.
- Return to 0.0 mm at 0.2 mm/s.
- If the rod specimen does not fail, repeat steps 1 and 2 four times.

Specimen NA3 survived four loading cycles without any sign of failure. The moment-curvature curves and equivalent stress-strain curves are shown in Fig. 11. In the estimates of equivalent stress and strain, the inside and outside diameters of 8.293 and 9.683 mm were used, respectively. There was a significant nonlinear deformation after 30 N·m; the maximum moment of 47 N·m was attained during the initial loading cycle. A deflection point appeared at approximately 8 N·m in the initial loading cycle. Subsequent loading cycles did not produce additional deformation, but they did introduce a closed hysteresis loop. The maximum curvature under a relative displacement of 24.00 mm at the loading points of the U-frame (i.e., 12.00 mm at each motor) was 4.1 m^{-1}. The maximum equivalent stress and strain obtained were 522 MPa and 2%, respectively. The rod appeared to be bent with significant plastic deformation after the static tests as shown in Fig. 12.
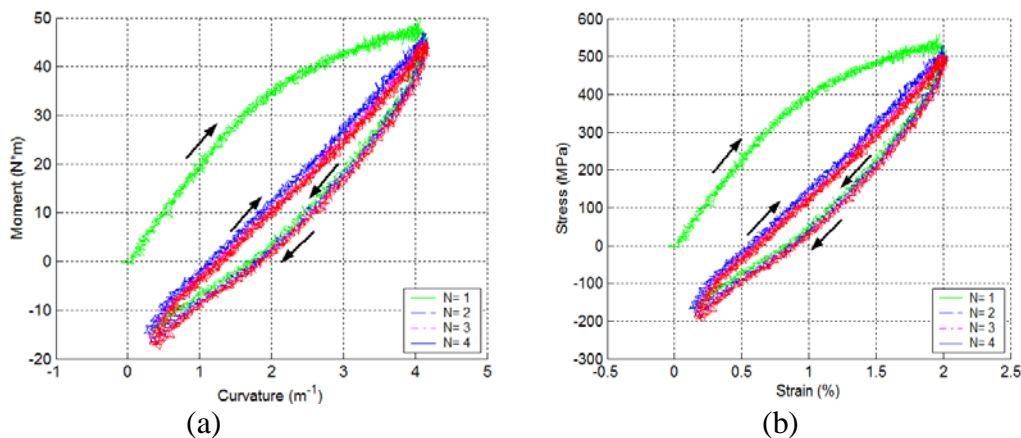

(a)   (b)

Fig. 11. (a) Moment-curvature curves and (b) equivalent stress-strain curves based on the first four loading cycles for specimen NA3 (651D3).
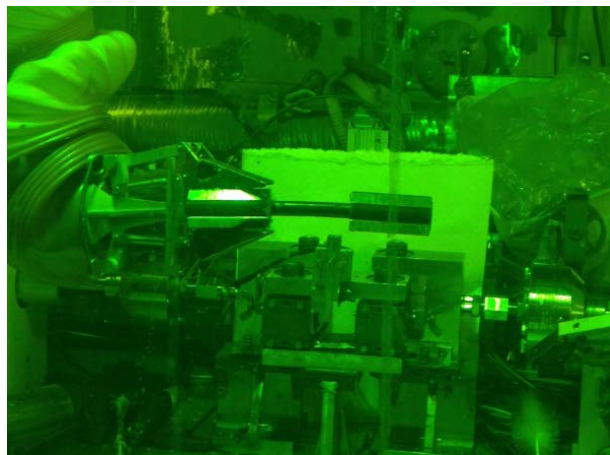

Fig. 12 Image of specimen NA3 (651D3) after testing; the rod sustained four cycles of loading to 24.00-mm relative displacement; the maximum moment with a level of 47 N·m was reached during the initial loading cycle.

V. CIRFT DYNMAIC TETSING RESULTS

5.1. HBR SNF Rod Test Results

Sixteen dynamic tests were conducted on the HBU HBR fuel in the hot cell, including one for benchmark testing and fifteen according to dynamic testing plan. Load amplitudes varied from ±5.08 to ±35.56 N·m; 12 tests were completed with specimen failure and 4 without failure. The fatigue life ranged from 5.5×10^3 to 2.3×10^6 cycles. The tests without failure were conducted under ±5.08 to ±8.89 N·m with the accumulated cycles beyond 6.4×10^6. Details of the typical dynamic tests results are described in this section.

5.1.1 D1 (607C4B) CIRFT Specimen

The test on D1 (607C4B, 63.8 GWd/MTU burnup, 70–100 μm oxide layer) was conducted under ±15.24 N·m, 5 Hz. A fatigue life of 1.1×10^5 cycles was obtained, and less than 1 gram of fuel fragments was collected at the failure site.

For each cyclic fatigue test, periodic quasi-static measurements of rod deformation were conducted using two relative displacement levels: 0.8 and 1.2 mm, at the target intervals described in Section 3.2. Time series of moment and curvature and moment-curvature loops obtained at the 1st cycle and after approximately 111,000 cycles are shown in Fig. 13. The loops became slender with accumulated cycles, and the amplitude of the loops decreased. The relations of moment-range versus curvature-range and flexural rigidity are illustrated in Fig. 14. Most of the rigidity degradation occurred in the first 1,000 cycles. Variations of these quantities as a function of number of cycles are provided in Fig. 15. Although the curvature range stayed quite consistent under displacement control, a decrease in moment range was observed. The rigidity of the measurements at two displacements, converged before the failure while exhibiting a slightly declining trend.

The curvature, moment, and flexural rigidity based on online monitoring data are presented in Fig. 16. The online monitoring showed a flexural rigidity of about 50 N·m^2, a little lower than that observed in measurements. This occurred because different loading conditions were used in measurement and cycling. A curvature range of less than 0.3 m^{-1} was used in the quasi-static measurement, which is lower than that used in the cyclic test to ensure measurement data didn't affect the dynamic cycle data. In general, the flexural rigidity tends to increase with decreasing curvature. This is probably due to a better interface bond at relatively low load resulting in less stiffness reduction. Overall, a stable rod response was exhibited before the final failure. The curvature time history shown in Fig. 18 (d), it clearly indicated a non-symmetric deformation under reverse loading, where the cladding tension site has much higher deformation (about 1.6 times) compared to that at cladding compression site. This phenomenon could be the consequence of debonding at the pellet-pellet interface and the stress concentration occurring at the pellet-pellet interface region at the tension side of the cladding, in addition to sensor probe sensitivity. In general flexural hysteresis history remains quite uniform throughout the reversal bending test, as shown in Fig. 18 (f). Under relatively low loading amplitude the clad or fuel pellet would be mainly under linear elastic behavior, the root cause of hysteresis energy dissipation under cyclic loading could be the system non-linear response associated with segment pellets induced stress concentration at interface regions as well as uncertainly resulting from sensor probe sensitivity.

Moment and curvature time history and moment-curvature loops based on online monitoring at 26 and 1.10×10^5 cycles are shown in Fig. 17. The curvature data appear to have a much higher noise level compared to that of out-of-cell surrogate rod test data. This is primarily due to there being two different calibration ranges for the LVDT set-ups used in the out-of-cell testing. The large range set-up is designated for static testing due to the large deformation required in that type of test, and the small range set-up which has higher sensitivity is designed for dynamic testing due to its lower test specimen
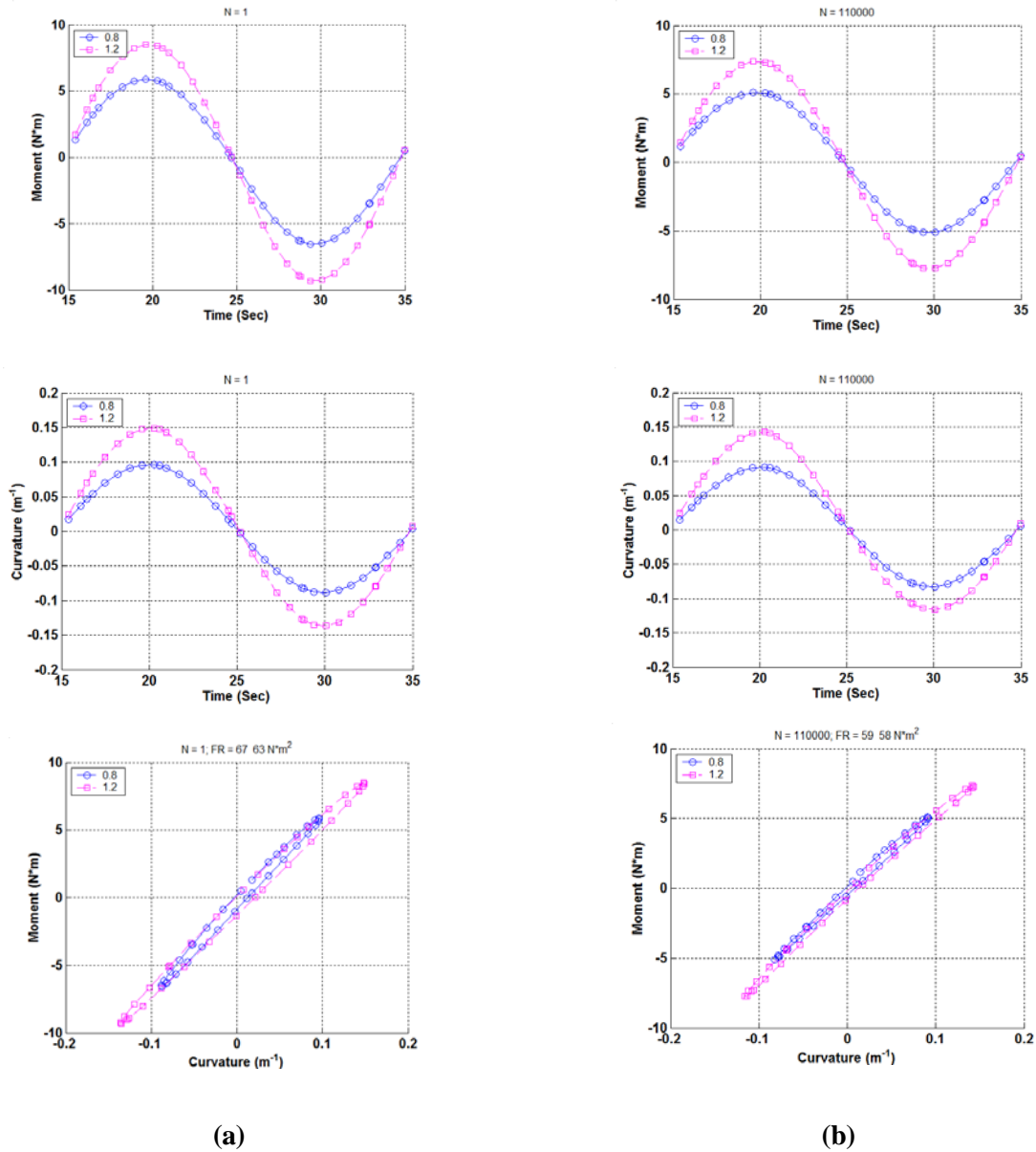
Fig. 13. Moment and curvature as a function of time and moment-curvature loops based on measurements when (a) N=1 and (b) N = 111,000 cycles for D1 (607C4B). Measurements were made with 0.8 and 1.2 mm relative displacements; N_f = 1.1×10^5 cycles under ±15.24 N·m, 5 Hz. Fuel particles collected <1.0 g.

deformation level. In a hot-cell environment, the current CIRFT device is only equipped with the large range calibration LVDT set-up, which is used to cover both static and dynamic testing capabilities. Thus, the sensitivity of the small range set-up for the low load dynamic testing was sacrificed, resulting in the higher noise level in the curvature data of Fig. 17. It is also noted that the symmetry curvature responses were observed at the beginning of cycles, which may indicate good interface bonds at the beginning of test cycle, while at higher cycling, the nonsymmetry characteristic of curvatures under clad tension and compression cycles was observed in Fig. 13.

The failure in test D1 was observed in the gage section near motor 2 (left side of the U-frame setup). The failure occurred at the pellet-to-pellet interface as illustrated in Fig.. The end faces of the two neighboring pellets were essentially clean. Both of the stressed cylinder surfaces of the rod were found to have been

12

covered with equally spaced circumferential cracks throughout the gage section. Spalling only occurred on the local area near the fracture. The degree of damage shown on both of the stressed cylinder surfaces of specimen D1 is different from the damage experienced in test specimens undergoing only unidirectional bending. The large deformation arising from the unidirectional bending can produce a greater extent of damage or spalling on one side of the test specimen with much less spalling on the other side of the specimen.

(a)

(b)
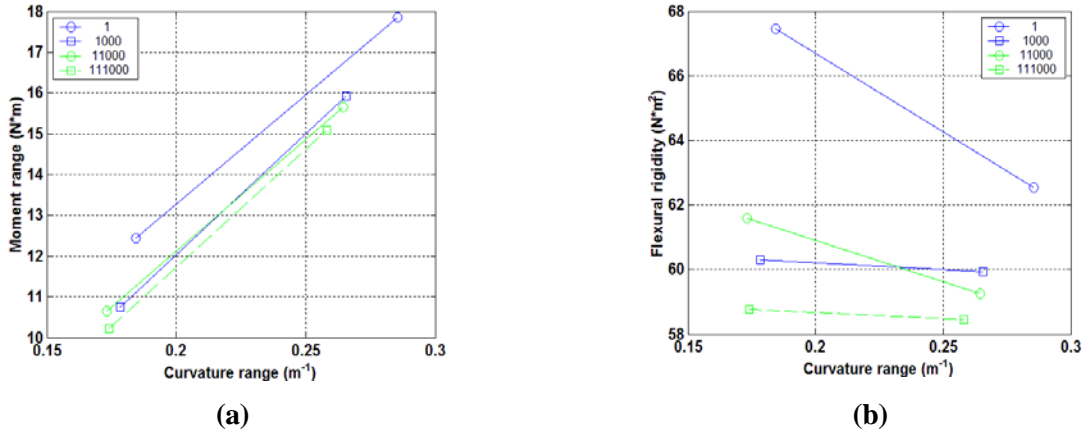
Fig. 14. (a) Moment-curvature relation and (b) moment-flexural rigidity relation at various numbers of cycles for D1 (607C4B); $N_f = 1.1 \times 10^5$ cycles under ±15.24 N·m, 5 Hz. Fuel particles collected <1.0 g.
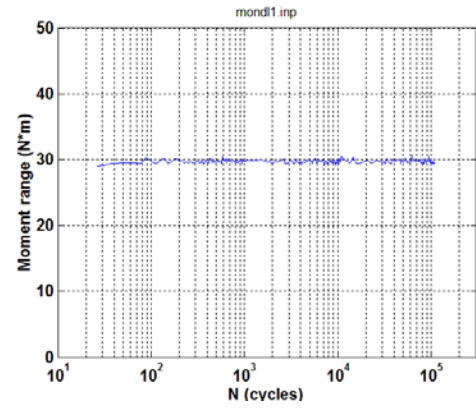

(a)

(b)

(c)
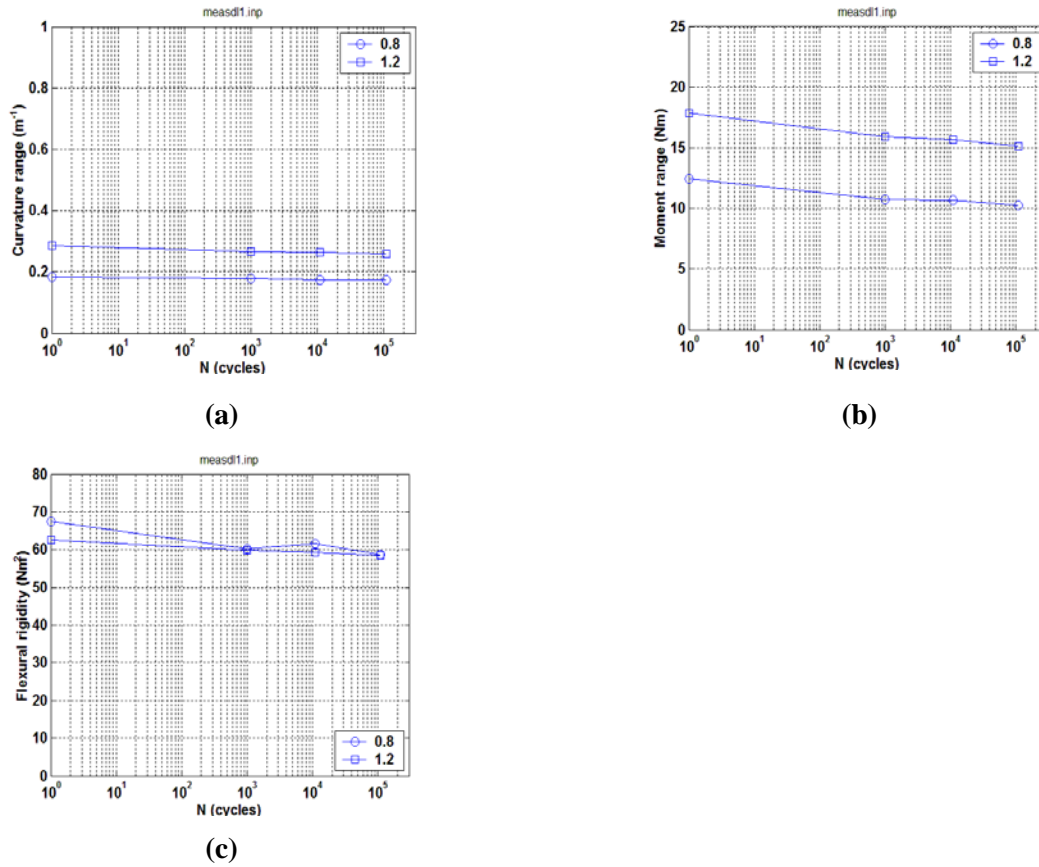
Fig. 15. Variations of (a) curvature range, (b) moment range, (c) flexural rigidity as a function of number of cycles for D1 (607C4B); $N_f = 1.1 \times 10^5$ cycles under ±15.24 N·m, 5 Hz. Fuel particles collected <1.0 g.

13
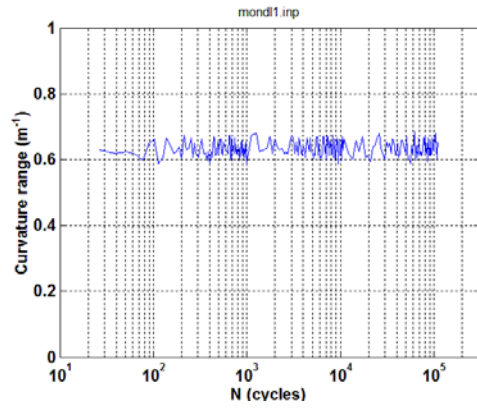
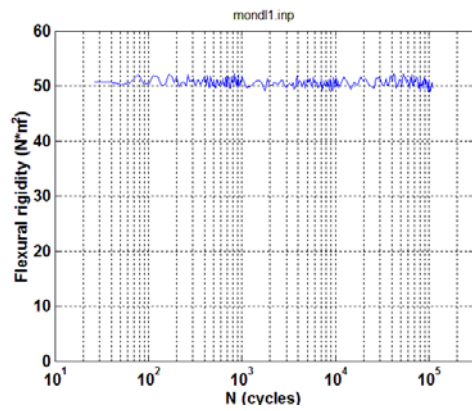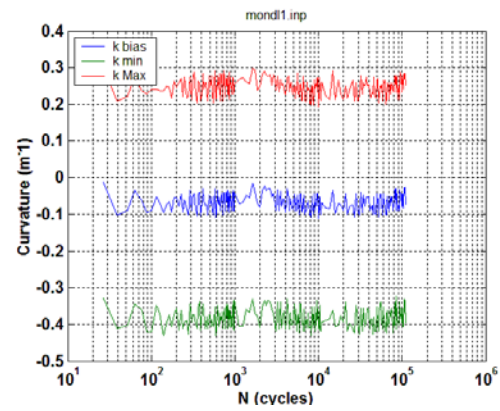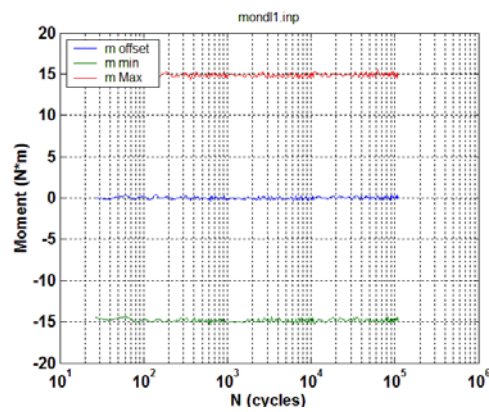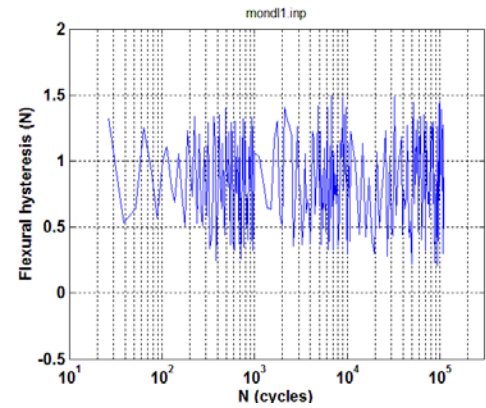**(a)**

(b)

(c)

(d)

(e)

(f)

Fig. 16. Variations of (a) curvature range, (b) applied moment range, (c) flexural rigidity, (d) maximum and minimum values of curvature, (e) maximum and minimum values of moment, and (f) flexural hysteresis as a function of number of cycles for D1 (607C4B); $N_f = 1.1 \times 10^5$ cycles under ±15.24 N·m, 5 Hz. Fuel particles collected <1.0 g.
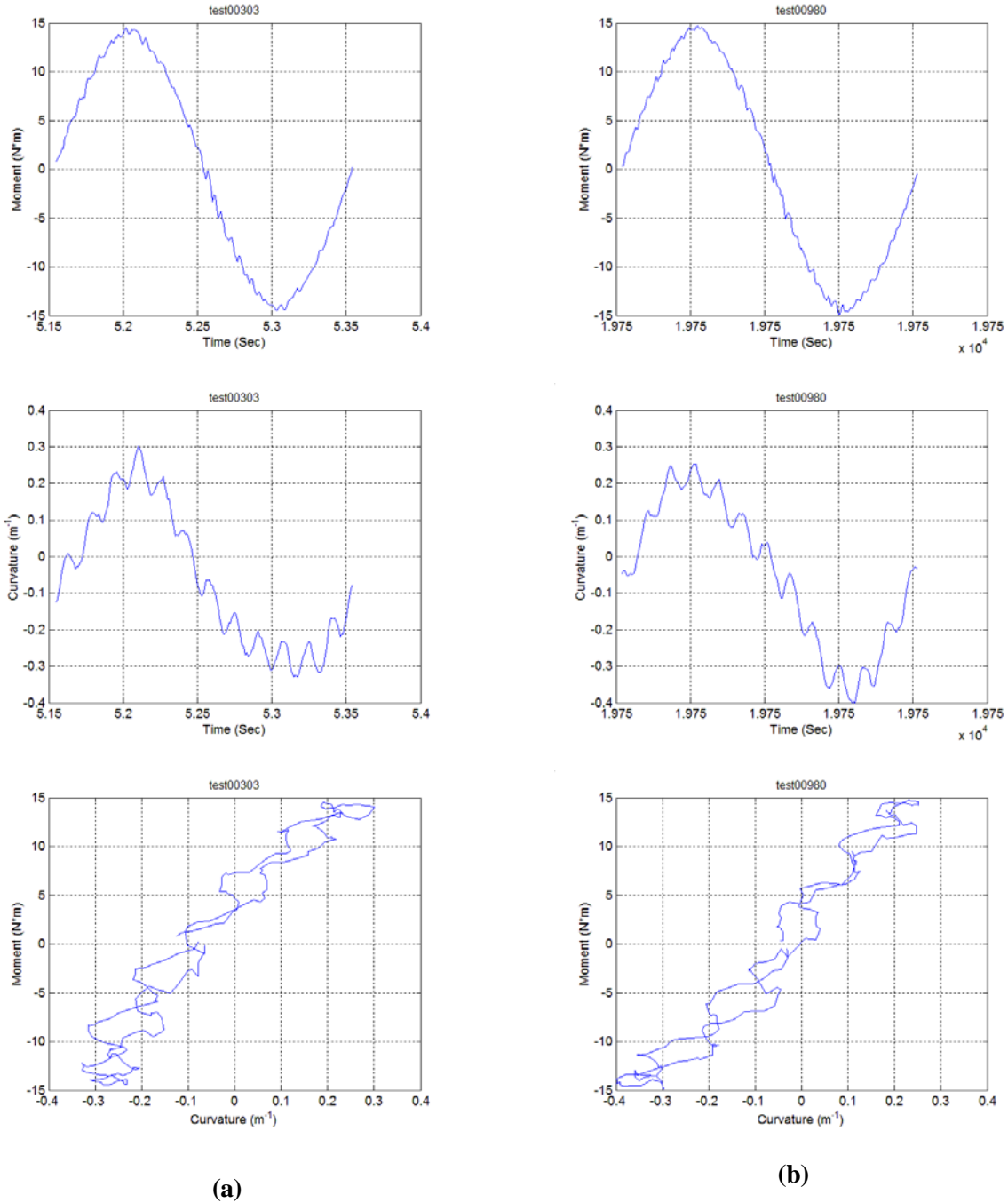
Fig. 17. Moment and curvature as a function of time and moment-curvature loops at (a) 26 and (b) 1.10×10^5 cycles; results are based on online monitoring.

5.1.2   S-N Fatigue Curve of HBR SNF Rods

The equivalent strain amplitudes (ε_a, half of strain range $\Delta\varepsilon$ /2, and equivalent strain ε is based on Eq. [3]) as a function of the number of failure cycles are shown in Fig. 19.

- For those specimens that failed during testing, the fatigue life decreases with increasing strain amplitude, resulting in a defined ε-N curve. The data points can be effectively fit by using the

15

(a)   **(b)**

(c)

(d)
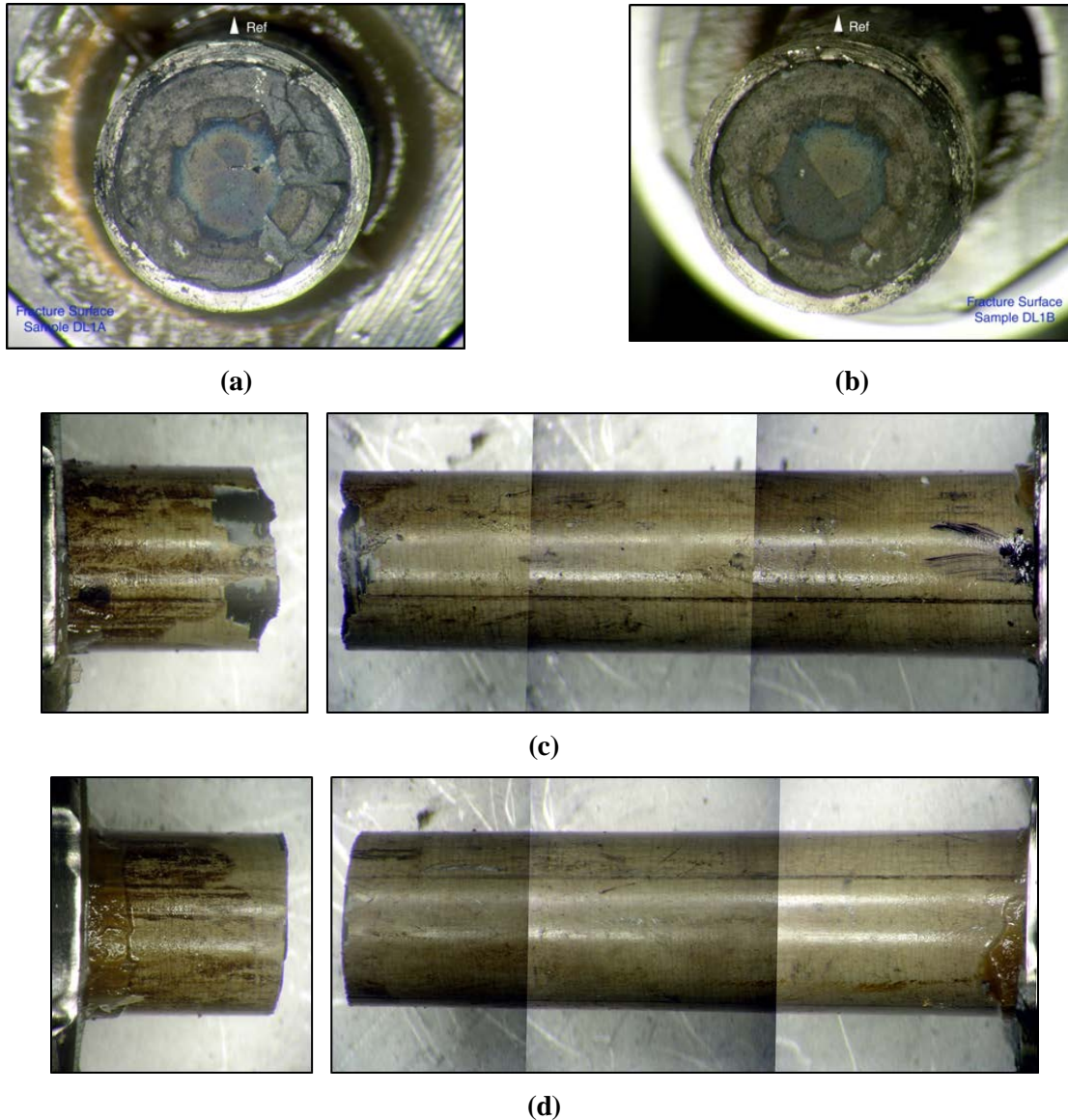
Fig.18. (a) and (b) Mating fracture surfaces, (c) frontal, and (d) back sides for D1 (607C4B), $N_f = 1.1 \times 10^5$ cycles under ±15.24 N·m, 5 Hz. Fuel particles collected <1.0 g.

  power function $y = 3.5693 \cdot x^{-0.252}$ with a correlation coefficient as high as 0.8722, where x is the number of cycles to failure and y is the strain amplitude (%).

- An endurance limit is likely located between 0.106 and 0.110% strains if it is defined at 10^7 cycles. In other words, below 0.1% strain amplitude there appears to be no number of cycles that will cause failure.

- A large variation of hydrogen content existed in the cladding of the test specimens in the dynamic tests. However, the contribution of hydrogen content to the number of cycles to failure appears to be secondary to the effect of imposed loading amplitudes.

The curve fitting to the strain amplitude versus number of cycles was extended to include the data points without failure by using two power functions, as presented in Fig. 20. For N ≤106, the power function was that based on failure data points, $y = 3.5693 \cdot x^{-0.252}$; for N >$10^6$, $y = 0.3234 \cdot x^{-0.076}$. It can be seen that the correlation efficient was quite lower for the second power function. This is because the amplitude is close to the endurance limit, and the number of failure cycles is likely independent of the applied load.
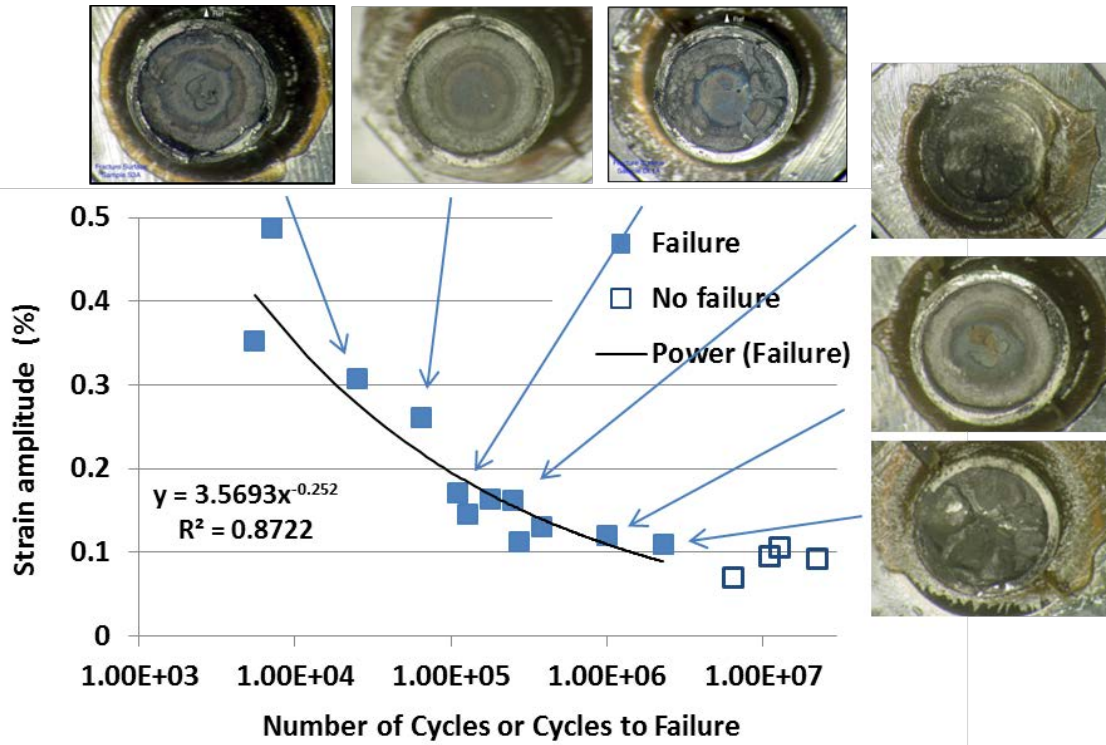
16

Fig. 19. Equivalent strain amplitudes ($\Delta\varepsilon/2$) as a function of number of cycles. Solid markers represent tests with specimens failure; open markers indicate the tests stopped without failure.
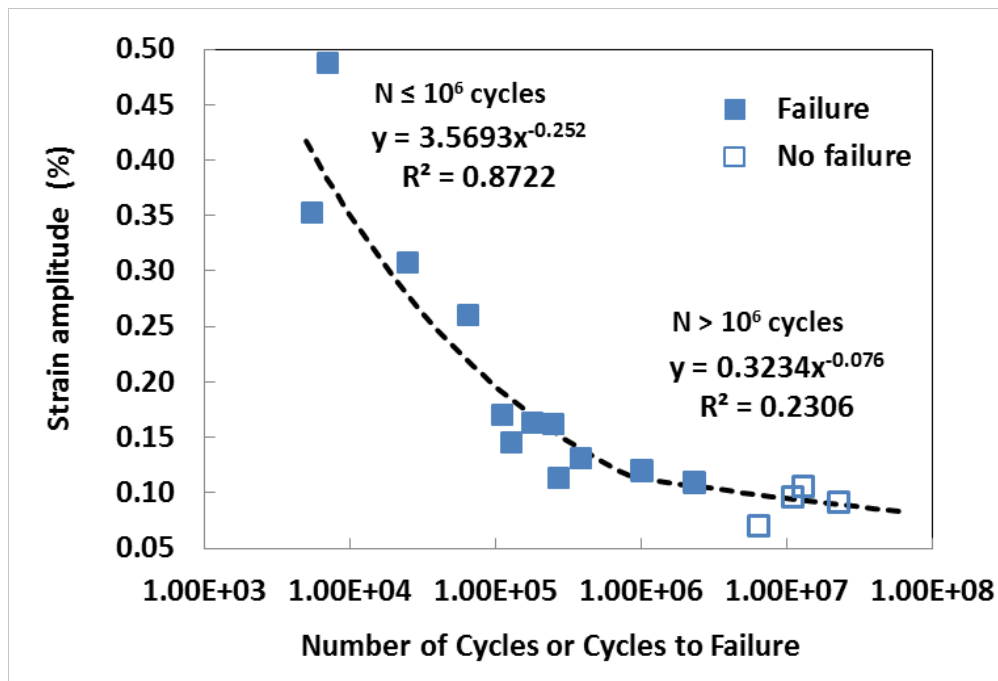

Fig. 20. Equivalent strain amplitudes ($\Delta\varepsilon/2$) as a function of number of cycles with curve fitting extended to include the data points without failure. Solid markers represent tests with specimens failure; open markers indicate the tests stopped without failure.

5.1.3 *Hydride Reorientation of HBR SNF Rods*

The objective of this hydride reorientation study is to collect experimental data on the hydride reorientation testing of HBR high burnup fuels under simulated conditions of SNF drying operations. Four CIRFT tests were completed on the HBR specimens with radial hydride treatment (RHT, 120 MPa hoop stress, 170 to 400°C, five cycles). Amplitudes ranging from 10.16 and 16.26 Nm were tested. One of the HBR RHT specimens (HR2) was tested under the following static conditions prior to dynamic testing: (1) six cycles of unidirectional bending with relative peak displacement 12 mm at U-frame loading points and (2) four cycles of fully reversed bending with relative peak/valley displacement +/-12 mm. This specimen apparently survived the static loading without failure and was then tested under dynamic loading. Due to a welded end-cap leak, only thermal heat treatment was applied to the HR4 sample.

The flexural rigidity of the rod specimens treated by hydride re-orientation was shown to be much lower than that of as-received specimens under equivalent amplitude. For example, under the same amplitude of 100 N, the rigidity of the RHT specimen (HR3) was only about 57% that of the as-received specimen (DL3). The variation of rigidity during a cyclic test was generally pretty continuous. In HR3, a sudden drop was observed prior to the failure.

The plots based on the mean values of quantities are given in Fig. 21 (a) to (b), where HBR1 represents the as-received specimen and HBR2 represents the specimen after radial hydride treatment (RHT). Note that the data of as-received HBR specimens were based on the original analysis method; namely, no correction was applied. It has been shown that the RHT reduces the fatigue life of SNF rods, as can be seen from the tests around 15 Nm. It was further observed that for HR2, as indicated by the arrow, there was an additional fatigue life reduction. Such reduction obviously resulted from the large-deformation static loading before the dynamic cyclic loading.
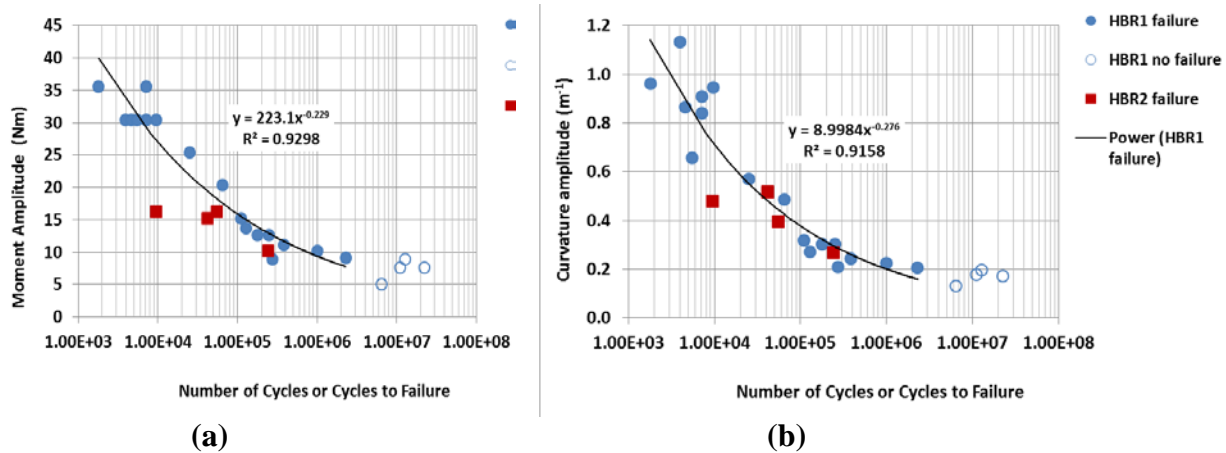

| (a) | (b) |

Fig.21. (a) Moment amplitude, (b) curvature amplitude, as a function of cycles or cycles to failure.

5.2 Limerick SNF Rod CIRFT Testing

14 SNF rod segments from the Limerick (LMK) boiling water reactor (BWR) were tested using the ORNL CIRFT equipment—one test under static conditions and 13 tests under dynamic loading conditions. Under static unidirectional loading, a moment of 85 N·m was obtained at a maximum curvature of 4.0 m^{-1}. The specimen did not show any sign of failure during three repeated loading cycles to a similar maximum curvature. Thirteen cyclic tests were conducted with load amplitudes varying from 25.4 to 7.1 N·m. Failure was observed in 12 of the tested rod specimens.

The cycles-to-failure ranged from 2.14×10^4 to 4.70×10^6. One cycled to 7.58×10^6 without failure, and the test was stopped. The measurements taken once the test was stopped indicated a range of flexural rigidity from 30 to 50 N·m^2. The online monitoring revealed that the flexural rigidity was slightly lower

18

due to the higher loading, from 25 to 42 N·m². This level of rigidity was a little lower than that of the PWR HBR specimens at 39 to 51 N·m². While the two claddings were based on Zircaloy-2 and Zircaloy-4, respectively, it is interesting to note that the geometrical sizes contribute more to the observed difference, where HBR rods had a relative smaller cladding outer diameter (OD) and pellet diameters compared to those of the Limerick BWR.

Thus, the observed higher rigidity of HBR pressurized water reactor (PWR) SNF may primarily be due to the higher strength of Zircaloy-4 cladding and higher pellet-clad interface bonding of the PWR pressurized environment. A BWR has about half the coolant pressure of a PWR.

In general, no substantial change of rigidity was observed based on the online monitoring during the cyclic fatigue testing process. Overall, the decreasing trend in lifetime with the increasing load amplitude is well defined. The LMK03 CIRFT test results are illustrated below to demonstrate typical LMK dynamic performance.

5.2.1. CIRFT Test on LMK03/575B-A

The test on LMK03/575B-A was conducted at ± 10.16 N·m, 5 Hz. The applied moment was higher than that of LMK02, and the lifetime of the specimen was accordingly longer at 4.92×10^5 cycles.

Periodic quasistatic measurements of rod deformation were conducted using two relative displacement levels (0.2 and 0.4 mm) at the selected target number of cycles. The variations in curvature range, moment range, and flexural rigidity as a function of number of cycles are given in Fig. 22. The rigidity of the measurements at the two displacements started with 44 to 48 N·m², dropped to less than 40 N·m² around 10^3 cycles, and remained nearly at a constant level afterwards.

The curvature, moment, and flexural rigidity based on online monitoring data are presented in Fig. 23. The online monitoring showed a flexural rigidity of about 35 N·m², a little lower than that observed in measurements. Again, an abrupt decrease in flexural rigidity was seen before the final failure.

The failure occurred in the gage section again as shown in Fig. 24. The failed specimen was manually broken into two pieces for fractographic study. The images of lateral surface and fracture surfaces are presented in

Fig. 25. Again, the fracture occurred on the pellet-to-pellet interface. Cracks developed in pellets, and pellets fractured into several large size fragments that were held in place. No apparent gap can be seen between the pellet and cladding. On the specimen ID side, a gray area can be seen. At this magnification level, it cannot be determined if the gray area is a damage area.
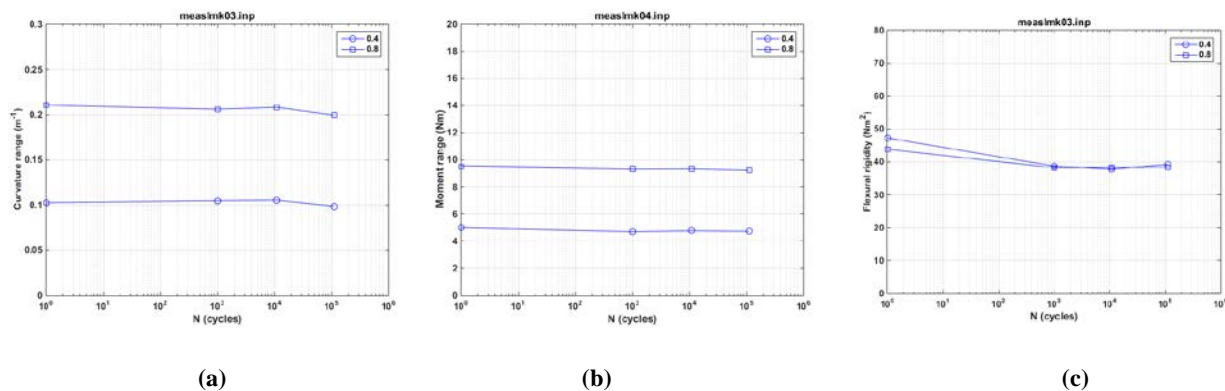

| (a) | (b) | (c) |

Fig. 22. Variations in (a) curvature range, (b) moment range, and (c) flexural rigidity as a function of the number of cycles for LMK03/575B-A; $N_f = 4.92 \times 10^5$ cycles at ±10.16 N·m, 5 Hz.

(a)   (b)   (c)
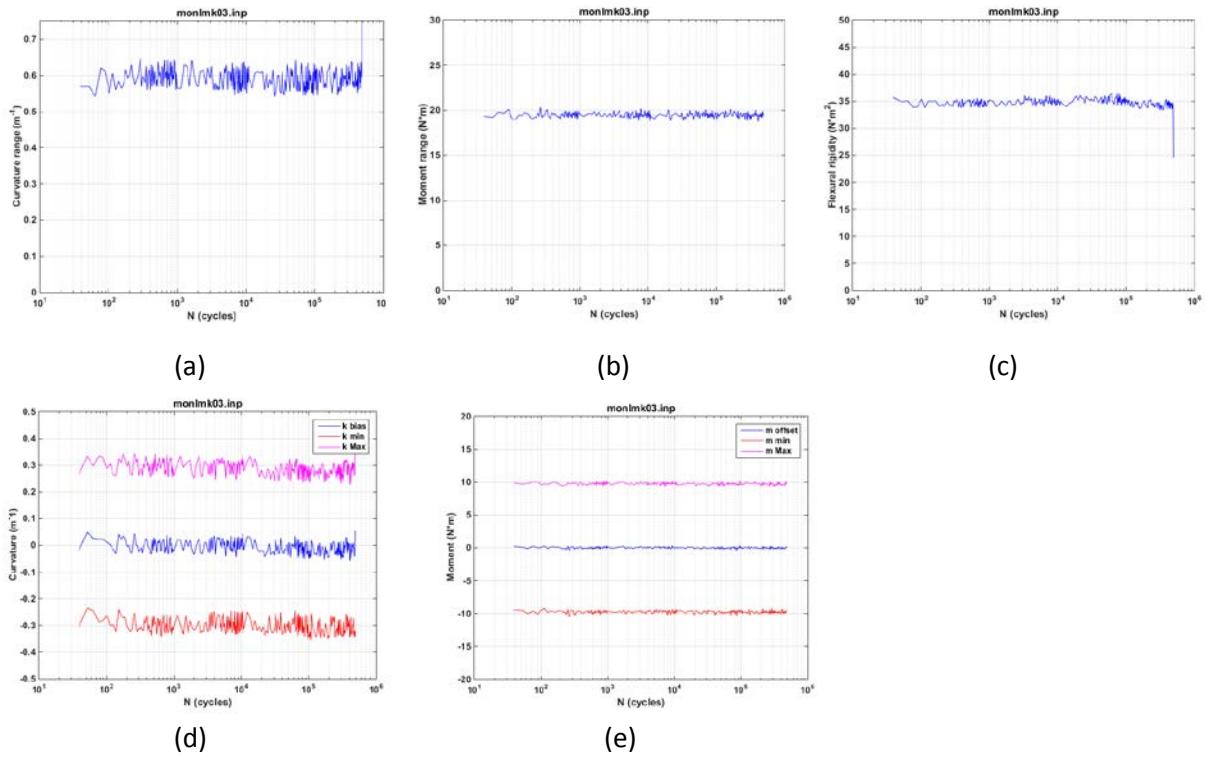

(d)   (e)

Fig. 23. Variations in (a) curvature range, (b) applied moment range, (c) flexural rigidity, (d) maximum and minimum values of curvature, and (e) maximum and minimum values of moment as a function of the number of cycles for LMK03/575B-A; $N_f = 4.92 \times 10^5$ cycles at ±10.16 N·m, 5 Hz.
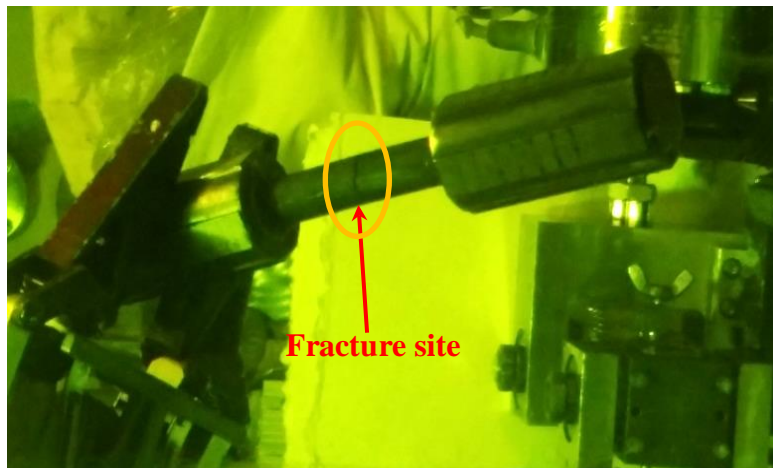

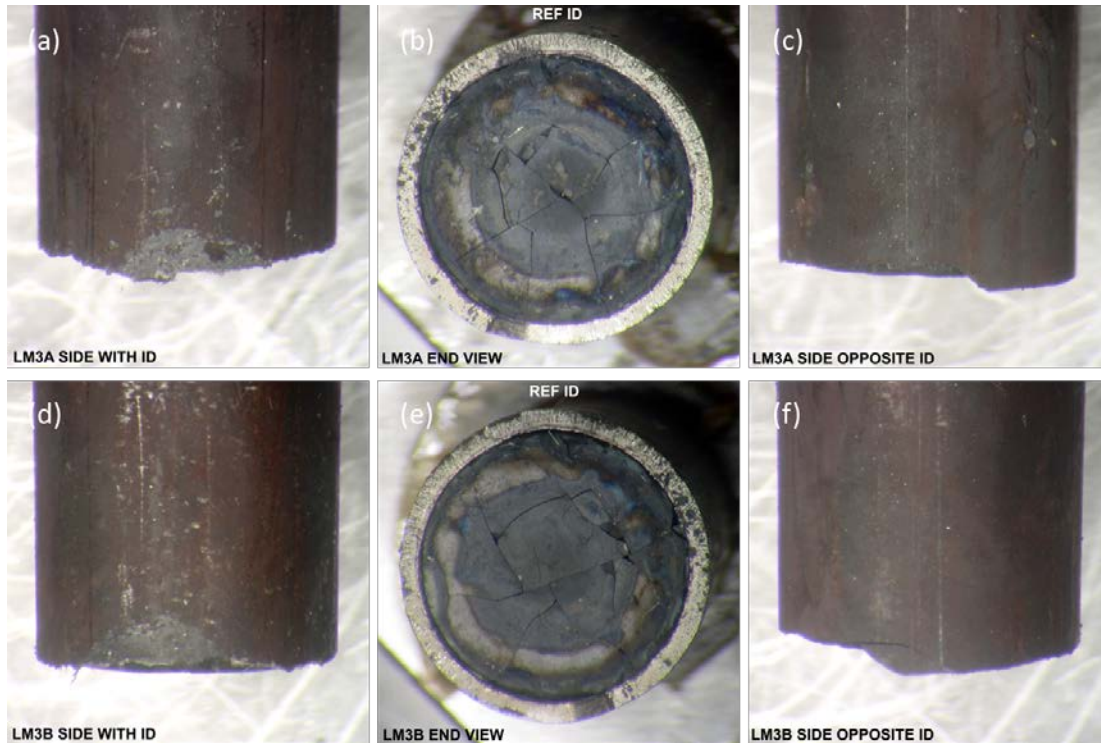
Fig. 24. Fracture segments for LMK03/575B-A $N_f = 4.92 \times 10^5$ cycles at ±10.16 N·m, 5 Hz.

Fig. 25. Fracture segments for LMK03/575B-A. (a) and (d) show the specimen ID side of the segment on end caps A and B; (b) and (e) show the mating fracture surface; and (c) and (f) show the opposite specimen ID side of the segment on end caps A and

VI.   INTERFACE BONDING EFFICIENCY STUDY FOR BWR AND PWR SNF RODS

Due to the inhomogeneous composite structure of the SNF system, finite-element analyses (FEAs) are needed to translate the global moment-curvature measurement into local stress-strain profiles for further investigation. Furthermore, the detailed mechanisms of the pellet-pellet and pellet-clad interactions and the stress concentration effects at the pellet-pellet interface cannot be readily obtained from a CIRFT system measurement. Therefore, detailed FEAs will be necessary for further interpretation of the global test response.

The FEA simulation focused on the BWR fuel rods and the results were compared with that of the PWR HBR fuel rods, which were validated and benchmarked using data from CIRFT. This paper provides analysis and conclusions concerning the pellet-pellet and pellet-clad interactions of SNF vibration performance, including (1) the distribution of moment-carrying capacity between pellets and clad and (2) the impact of clad material on the flexural rigidity of the fuel rod system. The immediate consequences of interface debonding are a shift in the load-carrying capacity from the fuel pellets to the clad and a reduction in the flexural rigidity of the composite rod system. Therefore, the flexural rigidity of the fuel rod and the bending moment resistance capacity between the clad and fuel pellets are highly dependent on the interface bonding efficiency at the pellet-pellet and pellet-clad interfaces. Furthermore, the curvature and associated flexural rigidity estimates based on tests conducted on the CIRFT system are very different from the localized clad data at the pellet-pellet interface region as estimated by FEA, where the local tensile clad curvature is approximately three to four times that of the global curvature at the tension side of the clad.

The initial comparison of bending flexural rigidity variation at different bonding efficiencies between PWR and BWR is summarized in Table 1.

Table 1 Flexural rigidity comparison of LMK BWR Zircaloy-2 clad and PWR HBR Zircaloy-4 clad

Interface bonding conditions	BWR flexural rigidity EI ($N \cdot m^2$)	PWR HBR flexural rigidity EI ($N \cdot m^2$)	Difference from BWR to PWR HBR (%)
Perfect bond	99	77	22
Pellet-pellet interface with gap debond, pellet-clad interface bonded	76	39	49
Pellet-pellet interface with gap debond, pellet-clad interface debonded	35	29	17
Pellet-pellet interface without gap debond, pellet-clad interface bonded	84	53	37
Pellet-pellet interface without gap debond, pellet-clad interface debonded	54	43	20

CIRFT test results indicate that the FEA-simulated BWR flexural rigidity was significantly overestimated, for perfect bond or partial debonding cases. This is because of the original UO_2 fuel property used in the BWR FEA study as well as the assumption made regarding the similar interface bonding efficiency between BWR and PWR environments. However, post-irradiation investigation (PIE) indicates that the BWR fuel pellet has more fracture intensity than that of the PWR fuel pellet; furthermore, PWR SNF should have a higher interface bonding efficiency than that of BWR fuel due to higher radial compressive residual stress induced by higher coolant pressure. Thus, the combined effect of BWR-degraded spent fuel and interface bonding deficiency was taken into consideration in follow-on FEA simulations by reducing the Young's modulus to 25% and 50% to quantify the interface bonding conditions that result in similar estimated rigidity to CIRFT SNF testing results, at pellet-pellet interface debond and pellet-clad interface bond conditions. The final BWR rod FEA simulation results are shown in Table 2, which indicate that updated FEA results, with consideration given to fuel module reductions, are more appropriate and consistent with those of CIRFT test results.

Table 2 Flexural rigidity comparison of BWR Zr-2 clad with fuel properties reduction consideration

Interface bonding conditions	Fuel UO_2 full E Flexural rigidity, EI ($N \cdot m^2$)	Fuel UO_2 ½ E Flexural rigidity, EI ($N \cdot m^2$)	Fuel UO_2 ¼ E Flexural rigidity, EI ($N \cdot m^2$)
Perfect bond	99	68	52
Pellet-pellet interface with gap debond, pellet-clad interface bonded	76	57	47
Pellet-pellet interface with gap debond, pellet-clad interface debonded	35	35	35
Pellet-pellet interface without gap debond, pellet-clad interface bonded	84	62	49
Pellet-pellet interface without gap debond, pellet-clad interface debonded	54	47	42

VII.   DISCUSSION

7.1   CIRFT Moment-Curvature Curves and SNF Fatigue Strength

The fatigue curves of Limerick rods were compared with those of HBR, NA, and MOX fuels in terms of amplitude of moment and strain, and results are given in Figs. 26 and 27. The strain amplitudes were obtained according to Eq. (3), $\varepsilon = \kappa \times y_{max}$ (where, κ is curvature and y_{max} is the radius of the cladding.). The data points for NA and MOX fuels are generally below the curve of moment amplitude versus N_f (cycles-to-failure, M-N curve) of HBR fuel, mainly due to the smaller cladding diameters of these fuels. Using strain amplitudes as a function of cycles will filter out some variability in SNF's dimensions and makes the data points from NA and MOX come close to M-N curve of HBR rods. Furthermore, due to the relatively lower rigidity of LMK compared to that of HBR, the LMK strain amplitude profile appeared to be above the HBR trend curve.

In order to further quantify or estimate the damage potential of the transient shock to the SNF vibration lifetime, a pilot study was carried out on MOX and LMK SNF. The CIRFT specimens were dropped two to three times from heights ranging from 1 to 2 ft to simulate the transient shock prior to initiating the CIRFT bending cycling test at a frequency of 5 Hz. The accelerated aging effects of the tested MOX and LMK CIRFT samples that had been dropped are shown in Fig. 26, marked with blue arrows. The LMK CIRFT rods that were dropped 1 ft at 10 N-m load show a 50% reduction in fatigue life. MOX CIRFT rods that were dropped 2 ft at 5 N-m load show a 73% reduction in fatigue life. Noted that one MOX rod at a 10 N-m loading level that had been dropped 2 ft does not show any accelerated aging. Due to variability of SNF rods and their inherent defect intensity, a more controlled CIRFT testing protocol needs to be included in the follow-on CIRFT high-rate testing program development.
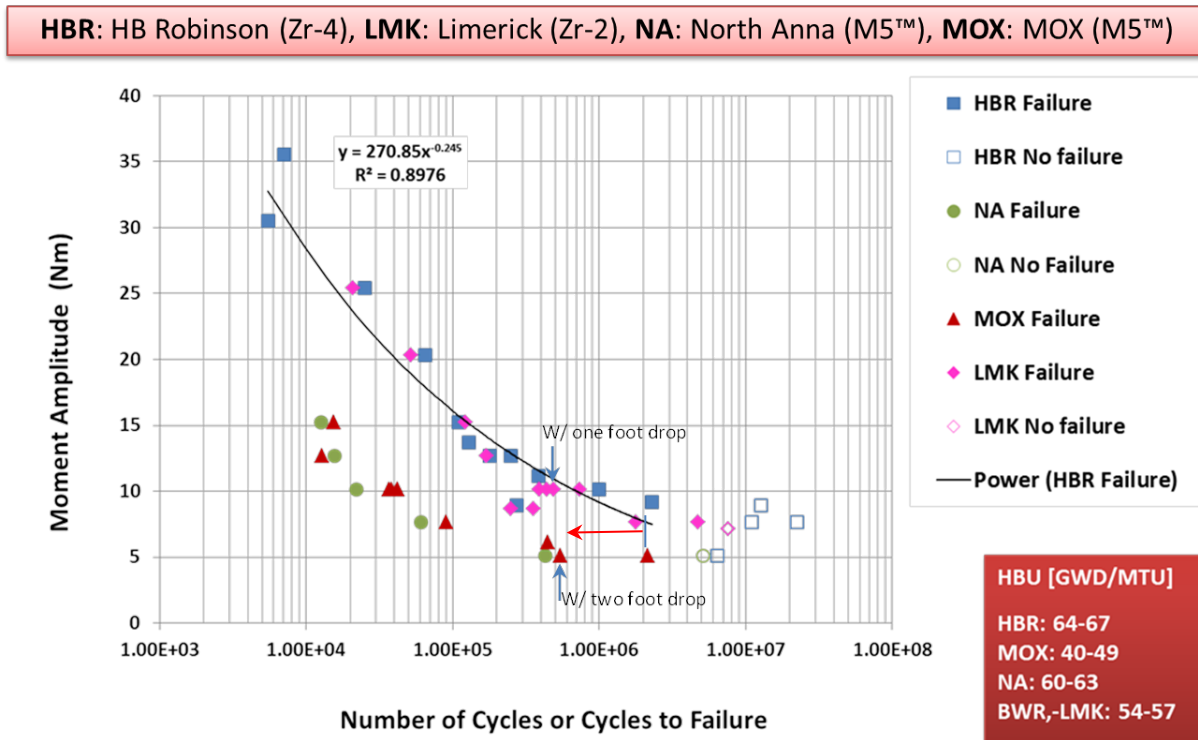

Fig. 26 Moment amplitudes as a function of number of cycles; results are based on CIRFT testing of various used fuels at 5 Hz. The power function was obtained from curve fitting based on the HBR data set. CIRFT fatigue test results reveal data scatter due to different types/sizes and burnup of clads tested.
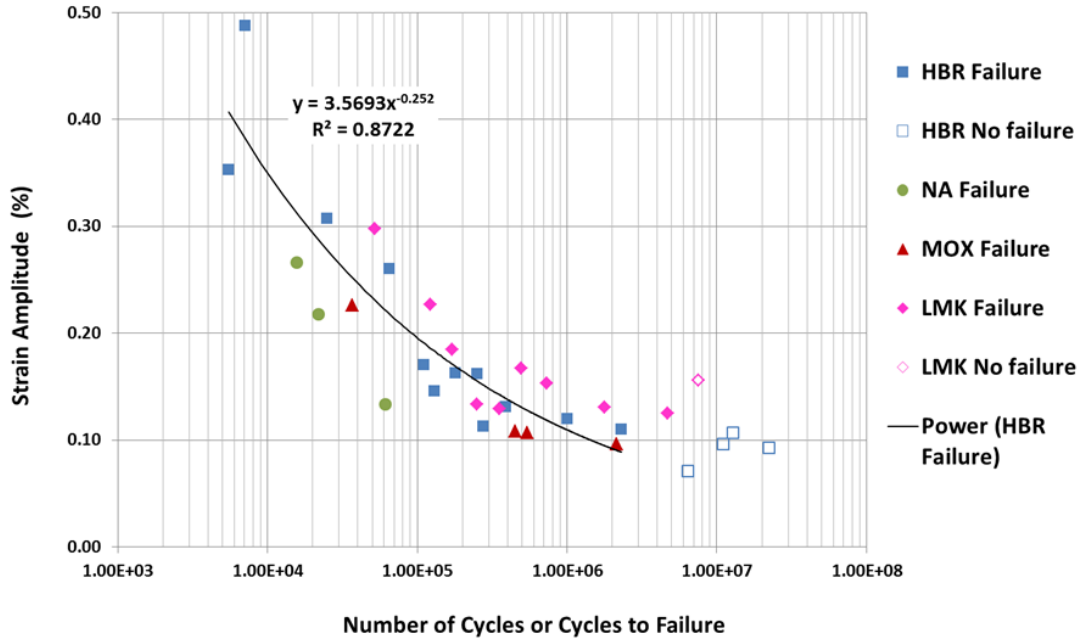
Fig. 27 Strain amplitudes as a function of number of cycles; results are based on CIRFT testing of various used fuels at 5 Hz. The power function was obtained from curve fitting based on the HBR data set.

VIII. CONCLUSION

This paper provides a detailed description of test results based on the CIRFT testing protocol used to determining the vibration integrity of a SNF rod under normal transportation conditions, especially in the realm of harmonic vibration. The CIRFT consists mainly of a U-frame testing setup and a real-time curvature measurement method. The three-component U-frame setup of the CIRFT has two rigid arms and linkages to a universal testing machine. The curvature of rod bending is obtained through a three-point deflection measurement method. Three linear variable differential transformers (LVDTs) are used and clamped to the side connecting plates of the U-frame to capture the deformation of the rod.

CIFRT test data provide new insights into SNF dynamic behavior. The CIRFT approach also successfully demonstrates the controllable fatigue fracture on HBU SNF in a normal vibration mode, which enables us to examine the underlying mechanism of SNF system dynamic performance. Lessons learned from CIRFT testing on SNF vibration integrity are summarized as follows.

- Fuel contribution to clad stiffness during random vibration
- Stress concentration effects on clad at pellet-pellet interfaces
- Relationship of flexural deformation mechanism to SNF rod aging history
- Potential hydrogen effects on SNF vibration integrity
- Pellet-clad bonding effects on SNF mechanical properties
- Finite element analysis is needed to translate CIRFT data into local stress-strain profiles
- Failure mechanisms of HBU SNF rods
- Potential impact of combined loading modes and loading rates
- PWR and BWR SNF vibration performance and the associated mechanical properties

REFERENCES

1. Jy-An Wang, Hong Wang, *Mechanical Fatigue Testing of High-Burnup Fuel for Transportation Applications,* NUREG/CR-7198, ORNL/TM-2014/214, May 2015.
2. H. E. Adkins et al., *Used Nuclear Fuel Loading and Structural Performance under Normal Conditions of Transport—Demonstration of Approach and Results of Used Fuel Performance Characterization,* FCRD-UFD-2013-000325, September 30, 2013.
3. J. Rashid, *Spent Fuel Transportation Applications—Assessment of Cladding Performance*, EPRI a Synthesis Report-1015048, December 2007.
4. P. McConnell, R. Wauneka, S. Saltzstein, and, K. Sorenson, *Normal Conditions of Transport Truck Test of a Surrogate Fuel Assembly*, FCRD-UFD-2014-000066, Sandia National Laboratories, August 29, 2014.
5. Jy-An Wang, Hao Jiang, and Hong Wang, *Dynamic Deformation Simulation of Spent Nuclear Fuel Assembly and CIRFT Deformation Sensor Stability Investigation,* ORNL/SPR-2015/662, November 2015.
6. Wang, J.-A. J., Wang, H., Yan, Y., Howard, R., and Bevard, B., High burn-up spent fuel vibration integrity study progress letter report (out-of-cell fatigue testing development – Task 2.1), ORNL/ TM-2010/288, Oak Ridge National Laboratory, Oak Ridge, Tenn., Jan 2011
7. J.-A. J. Wang, H. Wang, T. Cox, and Y. Yan, *Progress Letter Report on U-Frame Test Setup and Bending Fatigue Test for Vibration Integrity Study (Out-of-Cell Fatigue Testing Development–Task 2.3)*, ORNL/TM-2012/417, Oak Ridge National Laboratory, Oak Ridge, Tenn., August 2012.
8. J.-A. J. Wang, H. Wang, and T. Tan, *Reversal Bending Fatigue Testing*, Pub. No. US 2013/0205911 A1, Aug. 15, 2013; also as US Patent No. US 8,863,585 B2, Oct. 21, 2014.
9. H. Wang, J.-A. J. Wang, T. Tan, H. Jiang, T. S. Cox, R. L. Howard, B. B. Bevard, and M. E. Flanagan, "Development of U-frame Bending System for Studying the Vibration Integrity of Spent Nuclear Fuel," *Journal of Nuclear Materials,* **440**, 201–213 (2013).
10. J.-A. J. Wang, H. Wang, T. Cox, and C. Baldwin, *Progress Letter Report on Bending Fatigue Test System Development for Spent Nuclear Fuel Vibration Integrity Study (Out-of-Cell Fatigue Testing Development–Task 2.4)*, ORNL/TM-2013/225, Oak Ridge National Laboratory, Oak Ridge, Tenn., July 2013.
11. J.-A. J. Wang, H. Wang, B. B. Bevard, R. L. Howard, and M. E. Flanagan, *Reversible Bending Fatigue Test System for Investigating Vibration Integrity of Spent Nuclear Fuel During Transportation*, PATRAM 2013, DOE/NRC/DOT, San Francisco, Calif., August 18–23, 2013.
12. J.-A. J. Wang and H. Wang, *The Development of Reversible Bending Fatigue Tester and Its Application to High Burn-up Spent Nuclear Fuel Integrity Study under Normal Transportation Vibration*, ORNL/TM-2013/573, August 2014.
13. J.-A. Wang and H. Wang, *2014 Semi-Annual Progress Letter Report on Used Nuclear Fuel Integrity Study in Transportation Environments*, ORNL/TM-2014/63, April 2014.
14. J.-A. J. Wang, H. Wang and H. Jiang, *FY14 Status Report: CIRFT Testing Results on High Burnup UNF*, ORNL/LTR-2014/310, September 2014.
15. Jy-An Wang, Hong Wang, Hao Jiang, and Yong Yan, *CIRFT Testing of High-Burnup Used Nuclear Fuel Rods from Pressurized Water Reactor and Boiling Water Reactor Environments*, M2-FCRD-UFD-2015-000101, September 2015.
16. J. Geelhood, C. E. Beyer, and W. G. Luscher, PNNL Stress/Strain Correlation for Zircaloy, PNNL-17700, Pacific Northwest National Laboratory, Richland, Wash. July 2008.